IEEE Access
Multidisciplinary | Rapid Review | Open Access Journal

SPECIAL SECTION ON DEEP LEARNING ALGORITHMS FOR INTERNET OF MEDICAL THINGS

Received February 29, 2020, accepted March 15, 2020, date of publication March 19, 2020, date of current version March 31, 2020.

Digital Object Identifier 10.1109/ACCESS.2020.2982052

Negative Electrode Material Properties and Motion Safety of Wearable Medical Devices

XIANGBAI ZHANG[1] AND HUIJIE REN[2]
[1]Physical Education Institute, Hoseo University, Asan 31499, South Korea
[2]Physical Education Institute, Taiyuan University of Technology, Taiyuan 030600, China

Corresponding author: Huijie Ren (renhuijie1990@126.com)

ABSTRACT As health care has gradually become a hot research topic, the use of wearable medical devices to detect human exercise status and health indicators has become a focus of research. In this paper, lithium titanate materials with high safety and good structural stability were taken as the main research objects, and lithium titanate films with amorphous structure were studied. The film exhibited good electrochemical performance in the potential region of 0∼3 V, and the reversible capacity at 0.1 C was 283 mAh g-1, and only 3% of the capacity was lost after 100 charge and discharge. At a magnification of 5 C, the reversible capacity of the lithium titanate thin film reached 160 mAh g-1, and the loss rate after 100 charge and discharge was less than 7%. Based on EEMD (Ensemble Empirical Mode Decomposition), the intermuscular coherence was analyzed, and the characteristics of myoelectric signals were analyzed from different levels, and the muscle safety characteristics during exercise were estimated. Based on the test data analysis, the correlation between the average instantaneous frequency of sEMG (surface Electromyographic) and the intermuscular coupling characteristics during exercise is analyzed to provide a comprehensive evaluation method for muscle safety analysis. Finally, testing and analyzing the actual data to estimate the effectiveness of muscle safety provides a reference standard for the designation of exercise plans and the measurement of exercise volume.

INDEX TERMS Wearable medical devices, negative electrode film, electrochemical performance, muscle exercise safety analysis, myoelectric signal.

I. INTRODUCTION

With the rapid development of science and technology in the world today, the boundary between smart products and clothes is becoming increasingly blurred. Smart clothing can merge advanced electronics, communications, and computer software industries with each other, thereby opening up new markets for the traditional textile industry. At present, smart clothing has begun to be applied in various fields, such as sports equipment, health equipment, and game equipment. Wearable technology is a new application that has emerged in recent years [1]. It can be widely used in clinical fields such as clinical monitoring, family health care, sleep analysis, emergency care, and special population monitoring [2]. The so-called wearable application in the medical field is to integrate physiological information detection technology with clothing and accessories that people wear every day. Researchers have integrated medical sensor devices into rings, watches, clothing, etc., to make the wearer feel convenient and comfortable while detecting their physical parameters [3], [4]. The system can send the detected data at any time through wireless transmission, and analyse and process it to connect with the Internet, so that the monitoring center can keep abreast of the latest situation of the physiological system of the observed object.

In the 1950s, lithium metal primary batteries using lithium metal as the negative electrode, manganese oxide, carbon fluoride and silver vanadium oxide as cathode materials were successfully developed and gradually entered military and civilian use [5]. At present, a lithium battery which is generally used is a positive electrode material having a layered structure of lithium, and the layered structure of lithium can stably intercalate and deintercalate lithium at a high potential. This can be used as a negative electrode material and is capable of dissolving graphite and coke during the process of intercalating and deintercalating lithium at a low potential. The organic electrolyte with lithium salt is composed of three parts. When charging, negatively charged electrons come

The associate editor coordinating the review of this manuscript and approving it for publication was Wei Wei.

from the external circuit to the negative electrode, and positively charged lithium ions come from the inside of the battery to the negative electrode. The positively charged lithium ions are gradually embedded in the layers of the negative electrode material and combined with electrons to form a metastable structure of $LixC_6$. The discharge process is just the opposite.

With the improvement of living standards, people's attention to medical health, wearable physiological parameter monitors have gradually become a development hotspot [6]. A fabric-type breathing sensor developed by a related scholar has made a major breakthrough in the detection of respiratory rate [7]. However, there is still a certain gap between the current wearable medical monitors and the real integration into daily life, mainly due to the lack of a good motion interference removal technology. In the early products, the superposition averaging method was adopted [8], [9]. This method used the pulse wave to make the filter signal effect by repeatedly superimposing the motion signal entropy value which is randomly generated and the pulse signal is generated. However, this method is less used now because it requires a large number of periodic signals to participate in the addition and expectation to achieve good results. The researchers used acceleration sensors and matched adaptive algorithms to remove active noise from the physiological tester [10], [11]. The adaptive minimum-average method attempts to perform noise analysis from the photo-pulse signal itself and removes interference. The results show that the method is simple and suitable for general oximeters. The signal of physiological pulse wave is generally a signal with certain periodicity and specificity [12]–[14]. The frequency segments are concentrated in a certain range, and the motion signals are random and cover a large frequency range. Therefore, the wavelet denoising method has the characteristics of windowing, and the physiological signal can be moderately filtered. Researchers have dialected the time domain analysis method of ECG (Electrocardiograph) mutation signal, and determined that wavelet transform has a very obvious role in eliminating motion frequency interference [15]–[17]. Muscle physiology in exercise is an effective indicator of the amount of exercise, and the damage caused by excessive exercise is also the first to reflect the safety of the muscle [18]–[20]. Therefore, this paper will analyse the muscle safety status by collecting human sEMG (surface Electromyographic). The surface EMG signal can well reflect the degree of muscle safety, and has the advantages of non-invasive measurement, convenient acquisition, relatively small disturbance noise, etc., and is gradually applied to exercise safety monitoring. Since the generation and development of all devices serve human beings, smart wearable devices are no exception. They are closely related to human development. The use of wearable devices as medical devices to monitor the human body is currently a research hotspot. With the gradual change of medical concepts, the focus of medical research is no longer only on diseases, but health is also included in their research scope.

In this paper, a crystallized lithium titanate film and an amorphous lithium titanate film were prepared by ceramic target and powder target respectively, revealing the charge and discharge mechanism of amorphous lithium titanate film and crystallized lithium titanate film. The amorphous lithium titanate film has a wide operating voltage window and can be charged and discharged in a voltage range of 0 to 3 V, and has a high reversible capacity and a cycle retention ratio, and the energy density of the lithium titanate film can be further improved by nitriding. The EEMD (Ensemble Empirical Mode Decomposition) algorithm is used to obtain the IMF (Instantaneous Mean Frequency) of sEMG to reflect the variation trend of vibration frequency and amplitude of a certain muscle. Experimental results show that there is a positive correlation between the intermuscular coupling characteristics and the average instantaneous frequency IMF of sEMG. Therefore, using coherence indicators to comprehensively estimate muscle safety can reflect the change trend of muscle vibration frequency and amplitude in the safety process, and can also reflect the coupling characteristics between muscles, and can face the movement from different layers. Effective assessment of muscle safety changes enhances the reliability of muscle safety estimates.

The rest of this paper is organized as follows. Section 2 discusses related theories and methods. In Section 3, the performance of lithium titanate thin film electrodes for wearable medical devices was studied. Section 4 studies muscle exercise safety estimates for wearable medical devices. Finally, Section 5 concludes the study and finding, also the future work is included.

II. RELATED THEORIES AND METHODS

A. DATA FLOW PATH FOR WEARABLE MEDICAL DEVICES

The continuous flow of data and the self-quantification of users enable medical data to be presented to multiple parties, ultimately achieving the goal of improving the health of individual users or groups. These big data of health care wearable devices with many private content will be integrated and integrated multiple times to form a data lifecycle link belonging to health care wearable devices. Therefore, in addition to summarizing and analysing the data collected by health care wearable devices, analysing the complete data flow of health care wearable devices is also a very important part of exploring data security and privacy protection.

The data flow of the health care wearable device is based on the data collected by the health medical wearable device worn by the user, and the data collected by the health medical wearable device is sent to the health care service through various wireless networks. Combined with the flow of health care wearable device data, the data flow links can be divided into four parts: acquisition, uploading, integration interaction, and information feedback. Schematic diagram of the main flow links of wearable medical device data is shown in Figure 1.

The link of data flow in Figure 1 shows that health care wearable device data is an important object of

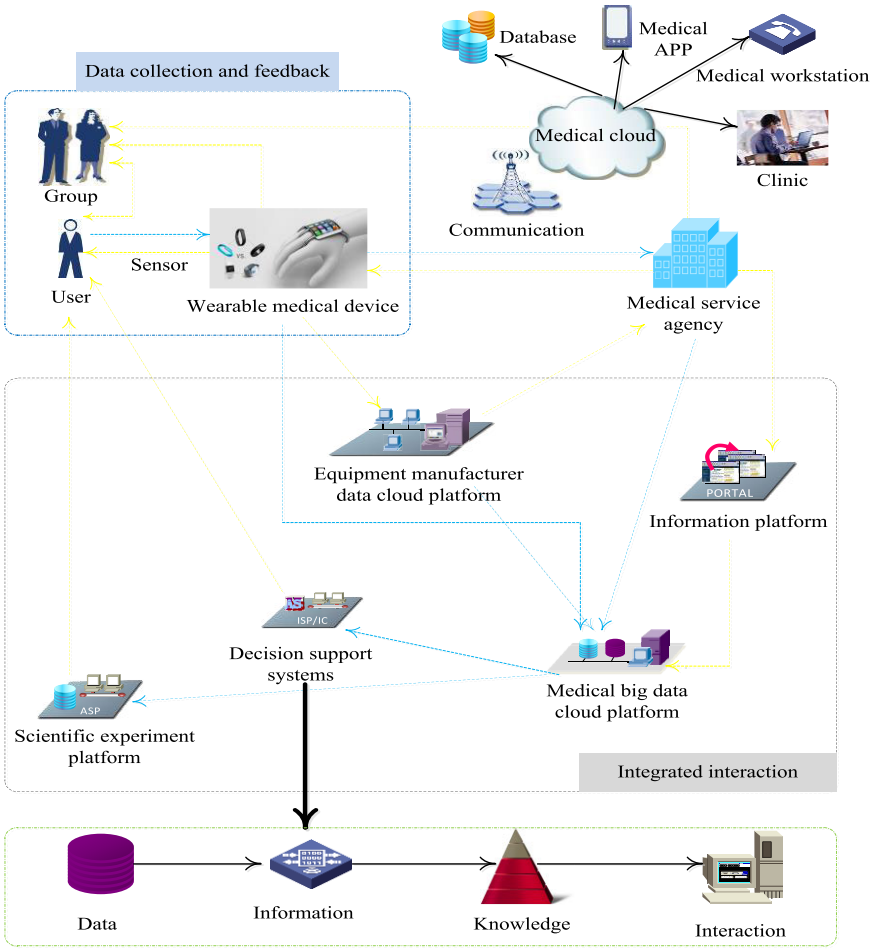

FIGURE 1. Schematic diagram of the main flow links of wearable medical device data.

interconnection. The data collection process mainly refers to the process in which the health care wearable device relies on the sensor to collect the user's personally identifiable information, vital signs, exercise behavior, emotional changes, and surrounding environment, and performs local storage in combination with the device itself. If the equipment manufacturer has a strong cloud platform as its support, the data may be retained by the cloud platform and then uploaded to the health care service information system. The health care big data cloud platform will also store the raw data before the integration.

B. TIME-FREQUENCY ANALYSIS METHOD OF MYOELECTRIC MOTION SIGNAL

Frequency domain analysis methods, such as Fourier transform, are suitable for the processing and analysis of stationary signals. The myoelectric motion signal is a non-stationary signal, so the individual time domain features and frequency domain features can not accurately describe the internal structure of the muscle, thus affecting the evaluation of muscle function status. In recent years, time-frequency analysis methods have begun to attract people's attention. The commonly used time-frequency analysis methods for myoelectric motion signals are STFT (Short-time Fourier Transform), WT (Wavelet Transform), WVD (Wigner-Ville Distribution), EMD (Empirical Mode Decomposition) and so on.

1) SHORT TIME FOURIER TRANSFORM

The short-time Fourier transform is based on the Fourier transform plus a window function, which is based on the Fourier transform multiplied by the time function g(t), and the input signal is x (t), then the STFT is calculated. The formula is as follows:

$$S_x^g(\tau, f) = \int_{-\infty}^{\infty} x(t) g^*(t-\tau) e^{-i2\pi ft} dt \tag{1}$$

Among them, $e^{-i2\pi ft}$ represents the frequency domain limitation, and $g^*(t-\tau)$ represents the time domain limitation, thus forming a time-frequency analysis method. However, the window function of the short-time Fourier transform is fixed. It cannot analyze the abrupt signal and is only suitable for the analysis of stationary signals, so it is not suitable for processing the surface EMG motion signal.

2) WIGNER DISTRIBUTION

The Wigner distribution represents the distribution of signal energy in the time-frequency domain. Its domain has the advantages of inversion and uniformity. It is more suitable for dealing with non-stationary signals. Let the input signal be x(t), then the Wigner distribution formula is as follows:

$$W_{PF_i}(t,f) = \int_{-\infty}^{\infty} x(t+\tau/2)x^*(t-\tau/2)\exp(-2\pi ft)d\tau \quad (2)$$

Among them, τ represents the delay time, t is the time, and f represents the signal frequency. Since the transformation of the Wigner distribution is two-line, when there are many components of the input signal, crossover between different components is easy, which causes artifacts.

3) WAVELET TRANSFORM

Wavelet decomposition is quite flexible in signal decomposition. Fourier transform has good local ability in the frequency domain, but it has no localization ability in the time domain, and wavelet decomposition has temporal local analysis ability. The characteristics of wavelet decomposition make it a good application in signal processing. Let the acquired EMG motion signal be x (t), and the wavelet decomposition is defined as follows:

$$W(s,\tau) = \int x(t)\varphi^*_{s,\tau}(t)dt \quad (3)$$

where ϕ represents the wavelet basis function.

After the wavelet basis function is stretched and translated, a wavelet sequence can be obtained, as shown below:

$$\phi_{s,\tau}(t) = \frac{1}{\sqrt{s}}\phi(\frac{t-\tau}{s})dt \quad (4)$$

The function that gets the wavelet decomposition is as follows:

$$W(s,\tau) = \frac{1}{\sqrt{s}}\int x(t)\varphi(\frac{t-\tau}{s})dt \quad (5)$$

where s represents the scaling factor.

When s is large, it is related to the low frequency component of the signal, but s is very small and is related to the high frequency component of the signal. $1/\sqrt{s}$ is used to store energy and is the process of continuous wavelet decomposition. The flexibility and fastness of wavelet decomposition is well applied in the analysis of bioelectrical signals, but the wavelet transform basis function selection lacks adaptability.

4) EMPIRICAL MODE DECOMPOSITION

EMD overcomes the shortcomings of Wigner distribution and wavelet transform. After EMD decomposition, the signal is decomposed into several intrinsic modal components. Each component represents a different frequency range, so the original EMG motion signal can be decomposed into different frequency bands after EMD decomposition. The signal obtains multiple intrinsic modal components after EMD decomposition. It calculates the average of the upper and lower envelopes to ensure that their mean is zero. If not, it re-executes the decomposition process until it is satisfied.

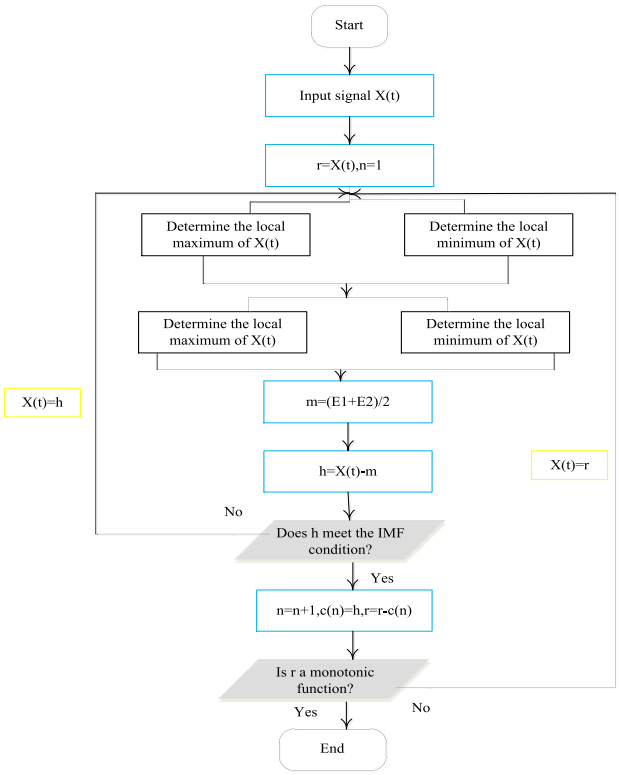

FIGURE 2. EMD decomposition process.

Let the original signal be x (t) and find the extreme points of the signal, namely the local minimum and the local maximum. Let the average of the upper and lower envelopes be m_1, and subtract this average from the original signal to find a new data function labeled h_1, ie:

$$h_1 = x(t) - m_1 \quad (6)$$

The number of marking cycles is k, and the first IMF component after decomposition is c_1. The first IMF component is removed from the original signal, and since the EMD is decomposed from high frequency to low frequency, a low frequency function is obtained, denoted as r_1:

$$r_1 = x(t) - c_1 \quad (7)$$

The second component of the EMD decomposition is denoted as c_2. After n executions, the n components of the original EMG motion signal after EMD decomposition are obtained. The algorithm flow of EMD decomposition is shown in Figure 2.

C. SOLID-STATE LITHIUM BATTERY AND THIN FILM ANODE MATERIAL

The electrolyte used in conventional lithium batteries is all liquid. The electrolytic solution is generally prepared by dissolving a lithium salt in an organic solvent. Conventional

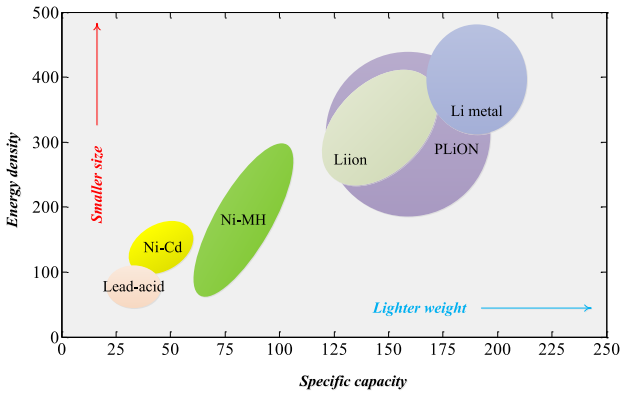

FIGURE 3. Comparison of energy density of various batteries.

lithium batteries have poor safety due to the relatively stable temperature range in which organic solvents are present. Although many companies have adopted methods such as adding flame retardants and high-temperature stabilizers to alleviate safety problems, they have not been able to eradicate safety hazards. Solid electrolytes have brought new developments to lithium batteries. Solid-state electrolytes have inherent safety features, which not only eliminate the safety hazards of lithium secondary batteries, but also improve energy density and miniaturization and thinning of batteries. At present, the use of solid-state lithium batteries in wearable devices and other portable electronic devices is gradually increasing. Due to the high energy density advantages of lithium-ion batteries compared to other batteries, the application and development of blowout applications have been ushered in the field of wearable devices such as smart watches and glasses. Figure 3 shows a comparison of the energy densities of various batteries.

Metal lithium is the most representative thin film anode material. The metal lithium film negative electrode is generally deposited on a thin film electrode material or a substrate by a thermal evaporation method under a vacuum environment, and has a theoretical specific capacity of up to 3500 mAh g^{-1}, which has been used by Japanese companies as an all-solid battery negative electrode. However, metallic lithium is very active, its melting point is only 180 °C, and it is very easy to react with water and oxygen. It is not suitable for using lithium metal as a negative electrode in the 250 °C reflow soldering process of many integrated circuits.

Lithium alloy materials are also typical thin film anode materials. The lithium alloy material not only has a high theoretical specific capacity, but also can reduce the electrochemical activity of lithium, reduce side reactions, and improve the safety of the battery. Since lithium is still a reactive ion, as the lithium ion is embedded, the electrode material undergoes a corresponding volume expansion. During use, the lithium metal alloy may have problems such as safety, structural collapse, and electrode powdering. Many researchers have reduced the volume change and mechanical stress in use by nano-alloying and preparing porous structural materials.

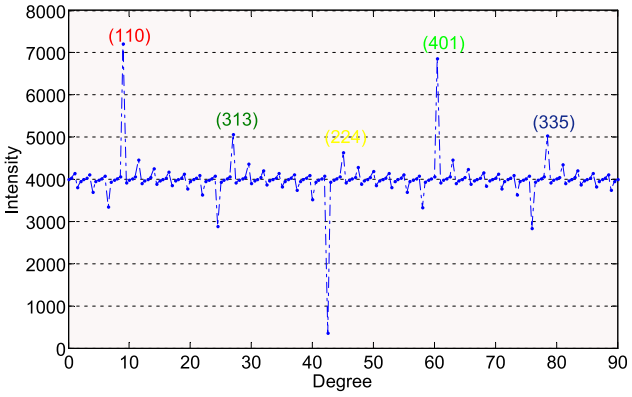

(a) XRD pattern of LTO powder

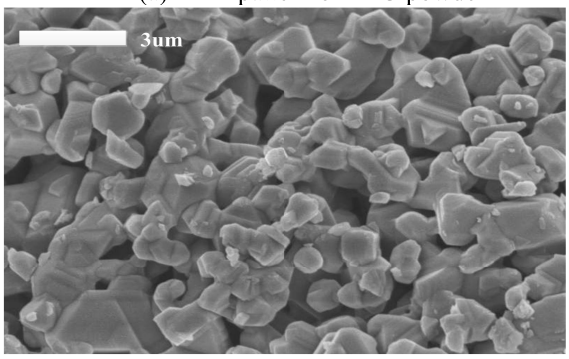

(b) SEM image of LTO powder

FIGURE 4. XRD and SEM images of LTO powder.

Moreover, researchers have used carbon fiber, graphene and other materials to modify and improve the alloy structure to solve the above problems.

III. PERFORMANCE STUDY OF LITHIUM TITANATE THIN FILM ELECTRODE IN WEARABLE MEDICAL EQUIPMENT

A. STRUCTURE AND MORPHOLOGY ANALYSIS

Figure 4 is a XRD (X-Ray Diffraction) and SEM (Scanning Electron Microscope) diagram of a sol-gel synthesized lithium titanate (Li4Ti5O12, LTO) powder. As can be seen from Figure 4(a), the LTO powder forms a distinct spinel structure, and the diffraction peaks and cards of the (110), (313), (224), (401), and (335) crystal faces can be very good coincidence. Figure 4(b) is a SEM photograph. It can be seen that the LTO powder has good dispersibility, uniform grain size and a particle size of about 1 um.

Figure 5 is an XRD pattern of an LTO film. It can be seen from the figure that the LTO film (C-LTO) prepared by the ceramic target has a relatively strong (110) crystal plane peak and a certain intensity of (313) and (224) crystal plane peaks, indicating the preparation of the ceramic target. The LTO film has undergone some degree of crystallization, as can be seen from the SEM image in Figure 5. At the same time, there is a weaker peak of titanium dioxide present in the LTO film prepared by the ceramic target. The LTO film (A-LTO) sample prepared from the powder target has only the peak of the stainless steel substrate, and there is no characteristic

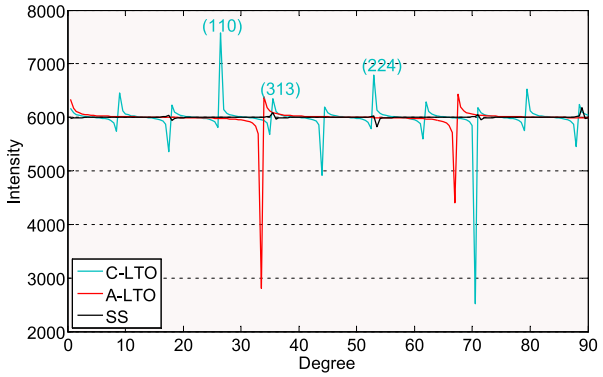

FIGURE 5. XRD pattern of substrate (SS), A-LTO, C-LTO.

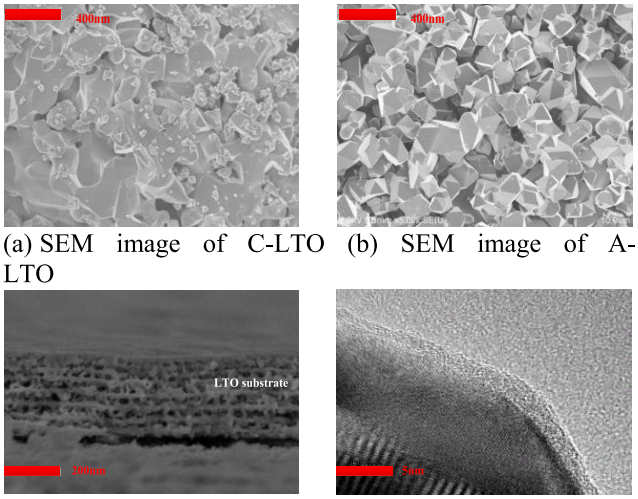

(a) SEM image of C-LTO (b) SEM image of A-LTO

(c) SEM cross-section of A-LTO (d) TEM image of A-LTO

FIGURE 6. SEM and TEM of LTO film.

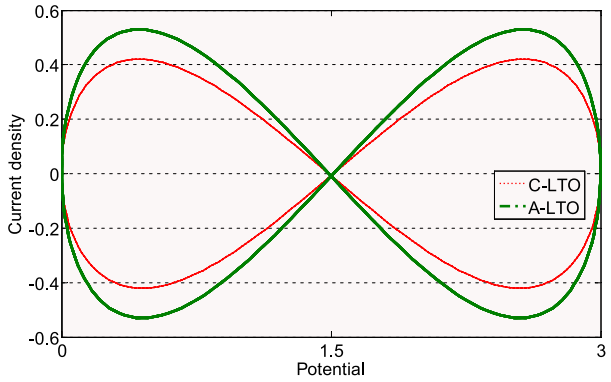

FIGURE 7. Cyclic voltammogram of LTO film.

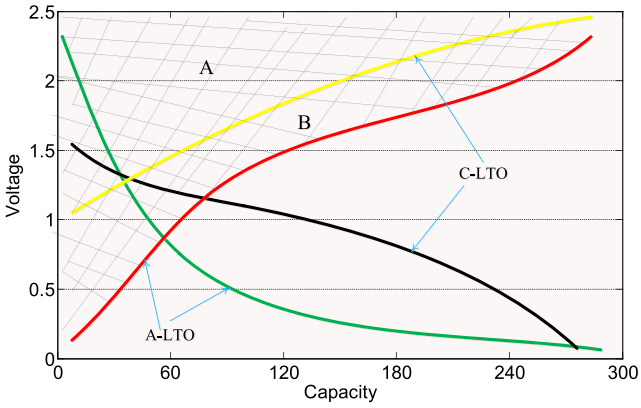

FIGURE 8. Comparison of charge and discharge of C-LTO and A-LTO films at 0∼3 V.

peak of any LTO film, indicating that the LTO film prepared by the powder target has an amorphous structure. It may be that the composition form of the molecular cluster of lithium titanate sputtered from the surface of the powder target is different from the composition form of the molecular cluster sputtered from the surface of the ceramic target, resulting in a lithium titanate film prepared by powder target. The amorphous structure of the film shortens the diffusion distance of lithium ions in the film particles, reduces the structural safety of lithium ions intercalating and deintercalating in the film, and improves the electrochemical performance of the film.

Figure 6 is a SEM and TEM photograph of the LTO film. As can be seen from the figure, the LTO film prepared by the ceramic target is a distinct crystal grain with a large crystal grain as shown in Figure 6(a). The LTO film sputtered by the powder target has no obvious crystal grain shape and the particles are fine, as shown in Figure 6(b). The LTO film prepared from the powder target shortens the transmission distance of lithium ions in the film and improves the electrochemical activity of LTO. In addition, the amorphous structure of the film provides a rich channel structure, making the electrolyte easier to immerse into the electrode material. The thickness of the LTO film sputtered by the powder target is about 110 nm, as shown in Figure 6(c). From Figure 6(d), the LTO film sputtered by the powder target did not show obvious lattice fringes, indicating that LTO is not crystallized or has a very low degree of crystallization, and is an amorphous structure film.

B. ELECTROCHEMICAL PERFORMANCE ANALYSIS OF LITHIUM TITANATE FILM

Figure 7 is a cyclic voltammogram of an amorphous LTO film sputtered by a ceramic target sputtered LTO film and powder target. The battery scan speed is 1 mV s^{-1}. The test temperature is room temperature. The crystallized LTO film exhibited a pair of typical spinel LTO redox peaks at 1.7 V and 1.2 V. The amorphous LTO film exhibits a pair of broadened LTO redox peaks in the potential range of 1.0 to 2.2 V and 0.3 to 1.2 V. The amorphous structure of the LTO film allows the intercalation and deintercalation of lithium ions to occur over a wide potential interval, and the shape of the charge and discharge curve is tilted without significant platform characteristics.

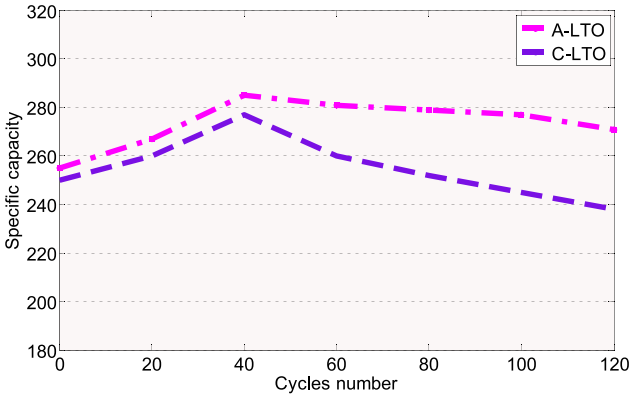

FIGURE 9. Cycle diagram of LTO film at 0∼3 V.

Figure 8 is a comparison of the charge and discharge curves of a crystalline LTO film prepared from a ceramic target and an amorphous LTO film prepared from a powder target at a 0.1 C rate. The test temperature is room temperature. The crystallized LTO film exhibits distinct plateau characteristics, and the charge and discharge curves of the amorphous LTO film are oblique. In the potential range of 0.7∼3 V, the specific capacity of the crystallized LTO film is about twice that of the amorphous film, but in the potential range of 0∼3 V, the specific capacity of the amorphous LTO film is significantly higher than that of the crystallized LTO film. The phenomenon that the spinel-type crystallized LTO film undergoes significant structural collapse due to charge and discharge in the potential range of 0∼3 V. The amorphous structure of the LTO thin film material exhibits a graphite-like lithium intercalation curve (green curve in the figure) during lithium ion intercalation, while in the lithium ion deintercalation process, the potential is slowly increased. In the case of lithium ion deintercalation, the potential is rapidly raised to above 1.5 V. As a negative electrode material similar to graphite, it is required that lithium ions can maintain a low potential as much as possible during the deintercalation process, so that a higher external output voltage can be exhibited when assembled with a positive electrode material. The shaded area A in the figure represents the increased energy density of the crystallized LTO during delithiation and lithium insertion. The shaded area A+B represents the increased energy density of the amorphous LTO during delithiation and lithium insertion. We know that amorphous LTO films provide higher energy density.

Figure 9 is a cycle life diagram of the C-LTO film and the amorphous LTO film at 0.1 C ratio in the 0 to 3 V range. As can be seen from the figure, the crystallized LTO film has a significant capacity reduction during multiple charge and discharge processes, and the maximum capacity is exhibited during the 39th discharge, and the attenuation is significant during the process of continued charge and discharge. The capacity after the 120th charge and discharge was about 18% lower than that at the 39th discharge. This indicates that the crystallized LTO has a structural collapse and a significant irreversible reaction during the deep charge and discharge of the voltage range of 0∼3 V, which causes the capacity to decay. The A-LTO film achieved a capacity of 285 mAh g^{-1} after the first few charge and discharge, and still maintained a capacity of 272 mAh g^{-1} after 120 charge and discharge, with a loss of only 4.5%. This shows that the amorphous structure of the LTO film can maintain structural stability during deep lithium insertion and delithiation, providing good cycle reversibility and high specific capacity.

IV. ESTIMATION OF MUSCLE EXERCISE SAFETY IN WEARABLE MEDICAL DEVICES

A. DATA ANALYSIS PROCESS

After preprocessing the EMG signals collected for each experimental period, the data analysis process is as follows:

(1) First, the pre-processed myoelectric signal is subjected to EEMD transformation. When EEMD is decomposed, the error is minimized in order to achieve the best separation effect. When N = 70 and the standard deviation of white noise is 0.39 times of the original signal, the separation is best.

(2) After the EEMD transformation, the instantaneous frequency corresponding to each moment is obtained, and for the entire test period, a one-dimensional array of myoelectric characteristics is obtained every 5% of the data segment.

(3) Using the array obtained in (2), we find the ratio of all the data in the array to the first data, and obtain the average instantaneous power ratio, root mean square ratio (root mean square ratio) and absolute standard deviation ratio of sEMG, where the three indicators reflect the change in the vibration frequency and amplitude of a muscle, so it can be used to estimate muscle safety.

(4) To illustrate the coupling characteristics between the muscles in the safety process, the coherence analysis of the two-channel EMG signals is performed as follows: 10% of each data segment is used as a segment during the entire experimental period to obtain two-channel muscles. The coherence threshold S is calculated, and finally the significant coherent area is obtained, denoted as A_1, A_2, A_3...A_{10}.

(5) When taking data segments in (2) and (4), we ensure that there is complete flexion and extension motion in each data segment.

B. SAFETY ESTIMATION BASED ON AVERAGE INSTANTANEOUS FREQUENCY

Taking the myoelectric signal collected by one of the subjects as an example, the EMG signals collected and decomposed by all subjects were decomposed and transformed. The instantaneous frequency corresponding to each moment is obtained by transformation.

Figure 10 shows the Hilbert spectrum after the EEMD decomposition and the Hilbert transform. It can be seen that the EMG signal can be transformed to obtain the instantaneous frequency of the EMG signal at different times, and the distribution is concentrated. After the pre-treated surface EMG signal passed the EEMD, 10 subjects were asked for

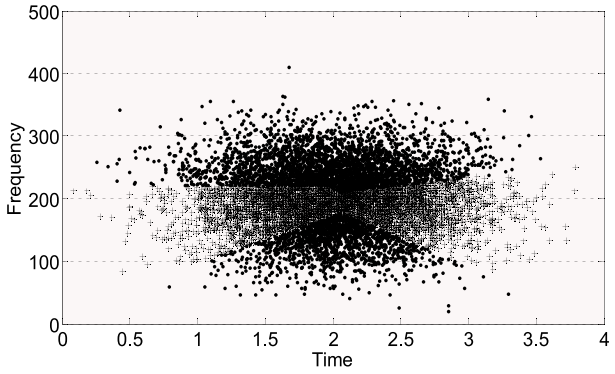

FIGURE 10. sEMG's Hilbert spectrum.

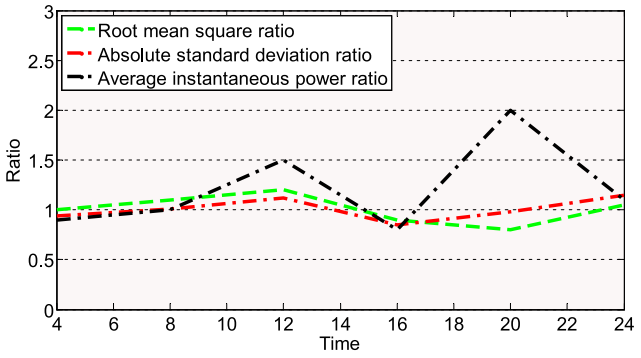

FIGURE 11. Trends in the values of sEMG.

the characteristic index. The entire test cycle is divided by 5% of the entire data length. Figure 11 shows the trend of the mean square root ratio, absolute standard deviation ratio, and average instantaneous power ratio of one of the subjects over the entire experimental period.

It can be seen from the figure that the ratio of the root mean square ratio to the absolute standard deviation at the beginning of the experiment is on the rise, and the change is not obvious. The average instantaneous power ratio of the surface EMG signal of the subject showed an upward trend before 12 s of the whole test period, and the average instantaneous power ratio appeared the lowest point at 16 s. In the 16-24s of the test period, the average instantaneous power ratio shows a trend of rising and then decreasing. Defining the first occurrence of the lowest point as a safe transition phase is meaningful in motion safety analysis. Using the same method to analyze other subjects, the average instantaneous power of sEMG is basically the same as the trend during the test period, and such a trend appears.

C. SAFETY ESTIMATION BASED ON COHERENT AREA

In order to describe muscle safety from the perspective of intermuscular coupling characteristics, coherence analysis was performed on two-channel EMG signals. The result is shown in Figure 12. The black thick line indicates the coherence threshold, and the portion exceeding the threshold is defined as significant coherence. Analysis of Figure 12 shows

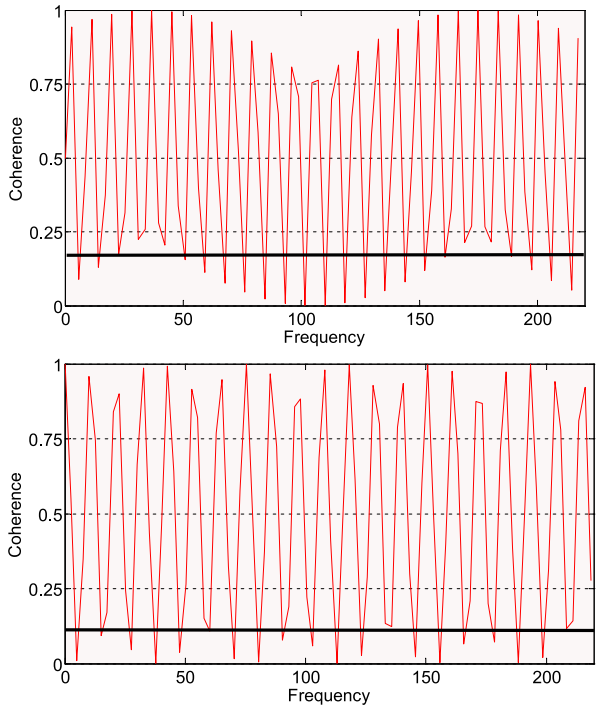

FIGURE 12. Results of A_1 and A_{10} intermuscular coherence analysis during the test period.

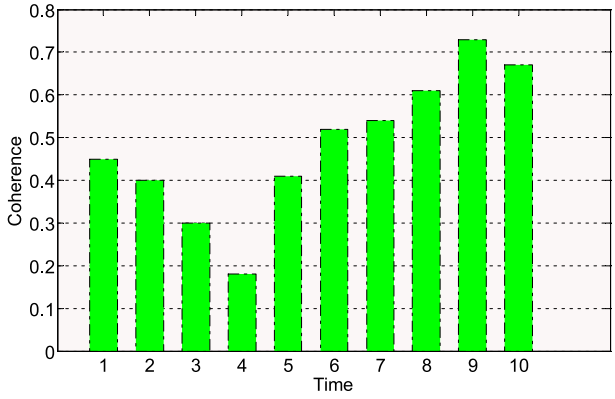

FIGURE 13. Coherence over time during the test period.

that the coherence between the two channels is significantly enhanced at the end of the test cycle. Through the coherence analysis between the EMG signals, the coupling characteristics between muscles can be reflected, and the motion safety state can be reflected from another aspect. It is indicated that the intermuscular coherence analysis can be used to estimate muscle movement safety.

In order to more intuitively express the law of coherence with time, the average value of intermuscular coherence in the frequency range is obtained for each piece of data of A_1, A_2, A_3...A_{10}, and the regularity of intermuscular coherence with time is obtained, as shown in Figure 13.

The subject described in Figure 13 showed a decrease in intermuscular coherence before 40% of the test period.

After 40% of the test period, the coherence was significantly enhanced, indicating that the intermuscular coherence was proportional to the degree of safety. This is consistent with the conclusion that there is a positive correlation between the safety of the study and the consistency of myoelectricity. In order to describe the change of coherence in time-frequency resolution, the test period is divided into three parts, namely, pre-test period, mid-test period and post-test period, and the coherence of time-frequency resolution is obtained for these three parts.

D. COMPREHENSIVE ANALYSIS OF SPORTS SAFETY

In order to quantitatively describe the trend of coherence in the safety process, the test cycle is divided into 10 segments for coherent analysis to obtain significant coherent area. At the same time, MIF (Mean Instance Frequency) is calculated, and the result is shown in Table 1.

In order to improve the reliability of the evaluation, the IMF significant coherence area of the sEMG obtained from 10 subjects. It can be seen from Table 1 that before 40% of the test period, the intermuscular coherence is relatively low and in a downward trend, at which time it has the same trend as the average instantaneous frequency of sEMG, indicating the intermuscular coherence at the beginning of the experiment. It has a certain relationship with the average instantaneous frequency of sEMG, and is positively correlated. When it exceeds 40% of the test period, the intermuscular coherence is significantly enhanced, and the average instantaneous frequency of sEMG also rises during the test period. At 60% of the time, sEMG's IMF once again reached its lowest point. This indicates that there is a positive correlation between the intermuscular coupling and the mean instantaneous frequency during the test period. Therefore, sEMG's IMF and intermuscular coherence can be used to estimate safety, which can reflect the trend of muscle vibration frequency in the safety process and reflect the coupling characteristics between muscles.

In order to further analyse the causes of intermuscular coherence and the average instantaneous frequency of myoelectric signals during the test period, the power spectrum of the EMG signal during the test period was calculated, as shown in Figure 14.

It can be seen from Figure 14 that the EMG signal is denser at 90% frequency. This is because it is relatively difficult for the subject to complete the designated task compared with the initial stage of the exercise, and thus it is necessary to exert all efforts, resulting in an increase in the number of exercise units and the activation frequency, and an increase in the energy of the myoelectric signal. As the exercise time increases, the coordination requirements between the muscles also increase, resulting in an increase in the coupling relationship between the muscles. This indicates that the intermuscular coherence is increasing with the degree of safety and has a

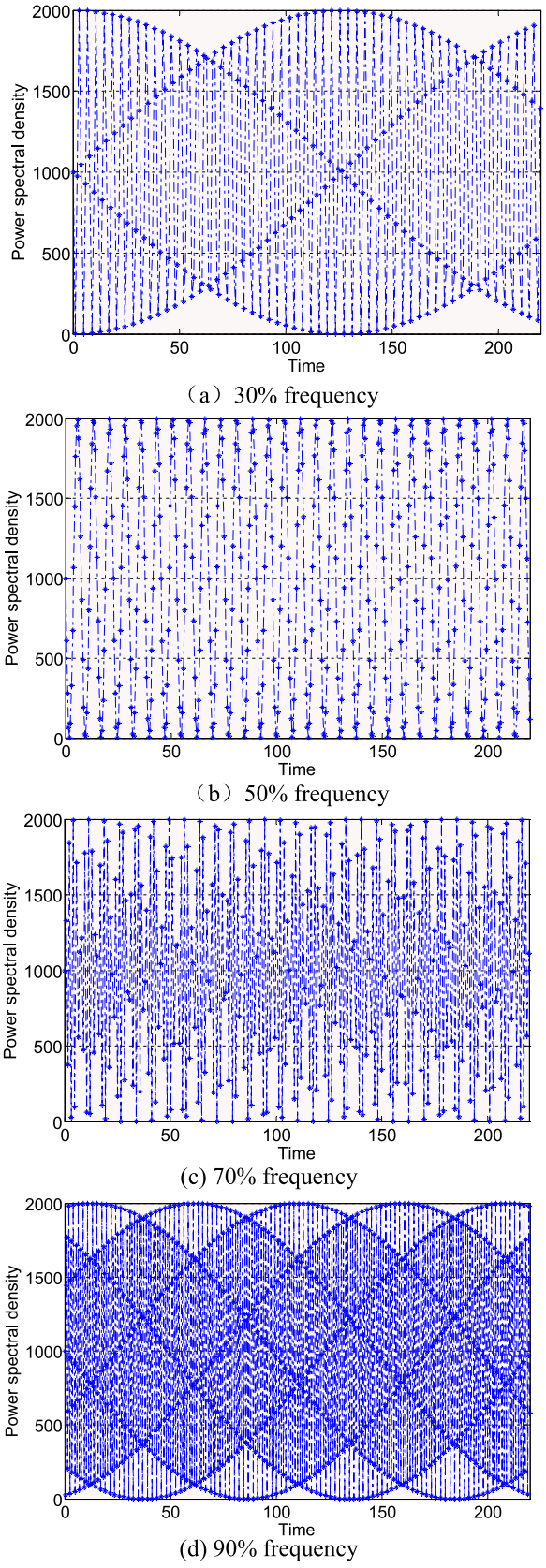

FIGURE 14. EMG signal power spectrum during the test period.

TABLE 1. Changes in indicators in the security process.

Cycle	10%	20%	30%	40%	50%	60%	70%	80%	90%	100%
Coherent area	37.2	35.3	19.9	3.7	31.9	50.8	56.9	75.7	96.2	82.5
MIF	1	1.3	0.9	2.4	1.6	-1.2	2.1	1.8	2.3	2.2

certain relationship with energy. Based on EEMD, the IMF of EPC and the coherence area of two-channel EMG signals are positively correlated with energy. The intermuscular coupling during exercise safety is related to the increase of muscle oscillation and the frequency of recruitment of motor units, and the muscle oscillation is inextricably linked with the IMF of sEMG, which makes the trend of IMF and coherence area of monom sEMG positive.

V. CONCLUSION

The application potential of all-solid-state thin-film batteries in wearable devices and micro-electronic devices is huge, and it is a key area to be broken. In this paper, the solid-state thin-film lithium battery is taken as the research background, and the negative electrode materials used in all-solid-state batteries are studied. The surface EMG signal contains a large amount of limb movement information, which can reflect the safety of human muscles. This paper studies the method of feature extraction, which is used to analyse the estimation of muscle safety during exercise and provide a basis for exercise safety.

In this paper, the LTO film structure of amorphous structure prepared by using lithium titanate powder target is relatively stable. The capacity and rate performance of the LTO film is further improved after nitriding. Part of the oxygen in the film is replaced by nitrogen to form a rich cross-linking structure, which improves the mobility of lithium ions in the film. In this paper, the intermuscular coherence model based on the EEMD Hilbert spectral analysis method is constructed. The characteristics of myoelectric signals are analysed from different levels, and the muscle safety characteristics during exercise are estimated. Based on the test data analysis, the correlation between the average instantaneous frequency of sEMG and the intermuscular coupling characteristics during exercise was studied, which provided a comprehensive evaluation method for muscle safety analysis. However, the motion feature extraction method studied in this paper is only for healthy people. The next step is to collect the patient's EMG signal and analyse the difference between normal people and patients, thus providing a more effective exercise safety evaluation method.

REFERENCES

[1] E. Rodriguez-Villegas, S. Iranmanesh, and S. A. Imtiaz, "Wearable medical devices: High-level system design considerations and tradeoffs," *IEEE Solid StateCircuits Mag.*, vol. 10, no. 4, pp. 43–52, Nov. 2018.

[2] A. Barsheshet, V. Kutyifa, T. Vamvouris, A. J. Moss, Y. Biton, L. Chen, E. Storozynsky, C. Wan, S. J. Szymkiewicz, and I. Goldenberg, "Study of the wearable cardioverter defibrillator in advanced heart-failure patients (SWIFT)," *J. Cardiovascular Electrophysiol.*, vol. 28, no. 7, pp. 778–784, Jul. 2017.

[3] R. Li, B. Nie, C. Zhai, J. Cao, J. Pan, Y.-W. Chi, and T. Pan, "Telemedical wearable sensing platform for management of chronic venous disorder," *Ann. Biomed. Eng.*, vol. 44, no. 7, pp. 2282–2291, Jul. 2016.

[4] P. M. Mohan, V. Nagarajan, and J. C. Vignesh, "Spot and continuous monitoring of heart rate by combining time and frequency domain analysis of photoplethysmographic signals at rest conditions," *IET Signal Process.*, vol. 11, no. 9, pp. 1076–1082, Dec. 2017.

[5] S. Zhou, X. Zhu, M. Zhang, D. Zheng, Y. Lei, Q. Zhang, S. Li, J. Driewer, S. Wang, and C. Enke, "SU-E-T-508: Internal organ motion effect on radiation dose to a point under half-beam block match line," *Med. Phys.*, vol. 42, no. 6, pp. 3451–3452, Jun. 2015.

[6] R. Kowalski, M. Capan, P. Lodato, D. Mosby, T. Thomas, R. Arnold, and K. Miller, "Optimizing usability and signal capture: A proactive risk assessment for the implementation of a wireless vital sign monitoring system," *J. Med. Eng. Technol.*, vol. 41, no. 8, pp. 623–629, Nov. 2017.

[7] T. Khurelbaatar, K. Kim, S. Lee, and Y. H. Kim, "Consistent accuracy in whole-body joint kinetics during gait using wearable inertial motion sensors and in-shoe pressure sensors," *Gait Posture*, vol. 42, no. 1, pp. 65–69, Jun. 2015.

[8] B. Lieber, B. E. S. Taylor, G. Appelboom, G. McKhann, and E. S. Connolly, "Motion sensors to assess and monitor medical and surgical management of parkinson disease," *World Neurosurg.*, vol. 84, no. 2, pp. 561–566, Aug. 2015.

[9] M. Shoaib, S. Bosch, O. Incel, H. Scholten, and P. Havinga, "Fusion of smartphone motion sensors for physical activity recognition," *Sensors*, vol. 14, no. 6, pp. 10146–10176, 2014.

[10] C. N. Teague, S. Hersek, H. Toreyin, M. L. Millard-Stafford, M. L. Jones, G. F. Kogler, M. N. Sawka, and O. T. Inan, "Novel methods for sensing acoustical emissions from the knee for wearable joint health assessment," *IEEE Trans. Biomed. Eng.*, vol. 63, no. 8, pp. 1581–1590, Aug. 2016.

[11] J. Unkelbach, "TU-AB-BRB-02: Stochastic programming methods for handling uncertainty and motion in IMRT planning," *Med. Phys.*, vol. 42, no. 6, p. 3586, Jun. 2015.

[12] S. M. Al-Khatib, P. Friedman, and K. A. Ellenbogen, "Defibrillators: Selecting the right device for the right patient," *Circulation*, vol. 134, no. 18, pp. 1390–1404, 2016.

[13] M. Hajibozorgi and N. Arjmand, "Sagittal range of motion of the thoracic spine using inertial tracking device and effect of measurement errors on model predictions," *J. Biomech.*, vol. 49, no. 6, pp. 913–918, Apr. 2016.

[14] H. Wang, X. Wang, and W. Chen, "Biomechanical comparison of interspinous distraction device and facet screw fixation system on the motion of lumbar spine: A finite element analysis," *Chin. Med. J.*, vol. 127, no. 11, pp. 2078–2084, 2014.

[15] H. Lee, J. Yoon, E. Lee, S. Cho, K. Park, W. Choi, J. Baek, K. Keum, and W. Koom, "SU-E-J-64: Feasibility study of surgical clips for fiducial tracking in CyberKnife system," *Med. Phys.*, vol. 42, no. 6, p. 3278, Jun. 2015.

[16] S. Ryu, P. Lee, J. B. Chou, R. Xu, R. Zhao, A. J. Hart, and S.-G. Kim, "Extremely elastic wearable carbon nanotube fiber strain sensor for monitoring of human motion," *ACS Nano*, vol. 9, no. 6, pp. 5929–5936, Jun. 2015.

[17] D. W. T. Wundersitz, C. Josman, R. Gupta, K. J. Netto, P. B. Gastin, and S. Robertson, "Classification of team sport activities using a single wearable tracking device," *J. Biomech.*, vol. 48, no. 15, pp. 3975–3981, Nov. 2015.

[18] J. Yoon, J. Jung, I. Yeo, J. Kim, and B. Yi, "SU-E-T-428: Feasibility study of 4D image reconstruction by organ motion vector extension based on portal images," *Med. Phys.*, vol. 42, no. 6, p. 3432, Jun. 2015.

[19] E. Tryggestad, "TU-F-BRB-01: Resolving and characterizing breathing motion for radiotherapy with MRI," *Med. Phys.*, vol. 42, no. 6, pp. 3625–3626, Jun. 2015.

[20] I. Jurkovic, S. Stathakis, Y. Li, A. Patel, J. Vincent, N. Papanikolaou, and P. Mavroidis, "SU-E-J-160: Motion analysis and 3D plane fit through the tumor center of mass positions in the 4DCT data set," *Med. Phys.*, vol. 42, no. 6, p. 3301, Jun. 2015.

XIANGBAI ZHANG was born in Hunan, China, in 1993. He received the master's degree from Yunnan Normal University, in June 2019. He will begin to study for the Ph.D. degree in physical education at Hoseo University. His research interest includes physical education.

HUIJIE REN was born in Shanxi, China, in 1990. He received the bachelor's degree from the Sports Institute, Shanxi Normal University, in 2012, the master's degree from the Postgraduate College, Shanxi Normal University, in 2015, and the Ph.D. degree from the Medical Science College, University of Dankook, South Korea, in 2019. He has published a total of ten articles in China and South Korea.